



OPEN

Modelling, characterization, and applications of silicon on insulator loop terminated asymmetric Mach Zehnder interferometer

Raghi S. El Shamy¹, Abdelrahman E. Afifi², Mohamed M. Badr¹ & Mohamed A. Swillam^{1✉}

This work presents a loop terminated asymmetric Mach–Zehnder interferometer (LT-aMZI) structure based on the widespread silicon-on-insulator (SOI) platform. Four different path length differences of the LT-aMZI, which correspond to free spectral ranges (FSR) from 0.8 to 6.4 nm, are designed. These designs are compared to the common asymmetric Mach–Zehnder interferometer (C-aMZI) and are shown to be more compact. These devices are suitable for optical filtering as well as wavelength demultiplexing (WDM) applications. A compact analytical model is derived that accurately describe the operation of the LT-MZI devices. The designs are then fabricated using Electron Beam Lithography (EBL) and characterized. The experimental data show good agreement when compared to the simulation results. To our knowledge, this is the first time LT-aMZI fabrication and characterization. Moreover, the LT-MZI spectrum can be tuned not only by the interferometer arms phase difference like C-MZI, but also by using its directional couplers coefficients, forming a spectral tunable filter. Finally, we determine the performance parameters of optical sensors and modulators and show that our proposed LT-MZI structure will enhance the sensor figure of merit (FOM) and modulator speed, power consumption and $V_{\pi} \times L$ compared to C-MZI. A comparison between symmetric and asymmetric MZI sensors and the advantage of the latter is also mentioned.

The rapid growth of Si-photonics industry over the past two decades, driven by the huge investments in the CMOS electronics industry, has made this new technology a potential cost effective solution for many new applications such as LIDAR systems¹, bio-sensing^{2,3}, hybrid photonic RF-ICs⁴, high speed and microwave signal processing^{5,6}, etc. Silicon on Insulator (SOI) is a widespread silicon photonics technology which supports submicron optical waveguides due to its high refractive index contrast. This platform supports many other optical components and devices such as Y-junctions, couplers, interferometers, gratings and resonators^{7–11} which form the building blocks of many photonic circuits and systems^{12,13}.

One of the most widely used optical devices is the Mach–Zehnder Interferometer (MZI). The simplest MZI configuration consists of two Y-junctions, one acts as a beam splitter and the other as a beam combiner and two waveguide arms. MZI is used in wide range of applications from wavelength division multiplexers¹⁴, optical switches^{15,16} and electro-optical modulators^{17–19} to biosensors^{20,21}. One of the advantages of MZI is its high immunity to temperature fluctuations when compared to resonators²². However, they suffer from large footprint. This large footprint become critical when many MZIs are required on the same chip and when very large length is necessary for achieving certain performance.

In this paper, we propose loop-terminated asymmetric MZI (LT-aMZI) design based on the widespread SOI technology. The LT-MZI is simply constructed from the conventional MZI with directional coupler (DC) splitter and combiner and a loop reflector^{23,24}. Our structure is the integrated version of the fiber reflection MZI (FRMZI) proposed by CA Millar et al.²⁵. This configuration allows the propagating light to travel back and forth in the interferometer arms rather than just once; resulting in smaller footprint and boost the performance of the conventional MZI in different applications. This paper is an exhaustive extension to our previously published work²⁶.

¹Department of Physics, The American University in Cairo, New Cairo 11835, Egypt. ²Electrical and Computer Engineering Department, The University of British Columbia, Vancouver, BC V6T 1Z4, Canada. ✉email: m.swillam@aucegypt.edu

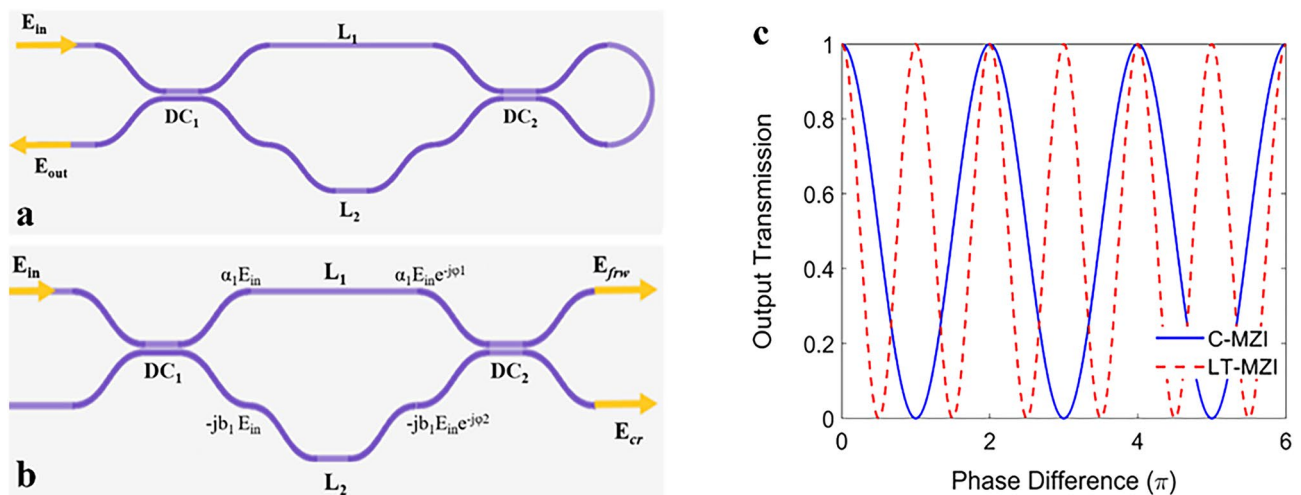


Figure 1. (a) Schematic of our proposed LT-aMZI, (b) schematic of C-aMZI, (c) output transmission versus interferometer arms phase difference of both LT-MZI and C-MZI with 3-dB directional couplers.

By integrating the structure presented in²⁵, several important advantages are added. Mass production using widespread CMOS process will result in significant reduction in the cost of such devices. In addition, easily on-chip integration of a whole system with source, detector and electronic parts allowing for compact handheld devices. Hence, integrated high performance optical sensors, electro-optical modulators and even gyroscopes using the loop reflector^{23,24} can be implemented using our structure. Similar structures to our proposed one were published previously. In^{27,28}, the same LT-MZI structure was presented but in the symmetric configuration and was used as a mirror with controllable reflectivity which then used by²⁷ to construct a Fabry–Perot cavity. While in²⁹ Michelson interferometer was proposed employing two loop mirrors compared to just one used in LT-MZI, i.e. more compact. Also, in³⁰ authors use asymmetric LT-MZI together with ring resonator to construct a Vernier sensor. Their work is based on numerical design and optimization using the transfer matrix method. Here we have derived a simple and compact analytical model that accurately describes the LT-aMZI structure rather than the complex transfer matrix method used in³⁰. Using our structure, we have designed optical filters and compared these designs with the common MZI showing our designs to be more compact. Simulation of the optical filter designs have been performed using Lumerical Interconnect³¹ which is fast circuit simulation software. These LT-aMZI designs have also been fabricated and characterized for the first time, with measurements showing good matching with Interconnect simulations as well as the analytical model. In addition, unlike conventional MZIs and Michelson interferometer in²⁹ the transmission spectrum of our proposed LT-MZI can be engineered using the DCs coupling coefficients and not just by the interferometer arms phase difference, which can be used as spectral tunable filter. Finally, using our compact model we show that our proposed LT-MZI structure enhance significantly the performance of optical sensors and electro-optical modulators that were using the widespread conventional MZI. Analysis also shows that the asymmetric MZI (aMZI) configuration offers an advantage over the symmetric MZI (sMZI) in sensing as both sensitivity and FOM can be engineered independently in aMZI, which is not applicable in the case of sMZI and also ring resonators.

Results

Structure and modeling. Our proposed loop terminated asymmetric Mach–Zehnder Interferometer (LT-aMZI) is shown in Fig. 1a, which is constructed from input directional coupler (DC) that split the input wave to the interferometer arms. The two interferometer arms experience different phase shift ϕ_1 and ϕ_2 and then another DC is used to combine the two arms waves. The outputs of the second DC are connected through a bend waveguide utilizing loop reflector as the one in^{23,24}. This loop reflect the waves back to the interferometer and the output is taken from the first DC as shown in Fig. 1a. Thus, our structure is constructed of a conventional MZI (C-MZI) using DCs, denoted as C-MZI_{DC}, and loop reflector. Hence, the transmission of our proposed LT-MZI can be derived using the C-MZI_{DC} forward t_{fw} and cross t_{cr} transmission coefficients shown in Fig. 1b.

The intensity transmission of our LT-MZI can be expressed as:

$$T_{LT-MZI} = |t_{LT-MZI}|^2 = A \left[\frac{H}{4} + \cos(\Delta\phi) \right]^2 \quad (1)$$

$$\text{where } A = 16a_1^2a_2^2b_1^2b_2^2 \quad (2a)$$

$$\text{and } H = -\frac{a_1a_2}{b_1b_2} - \frac{b_1b_2}{a_1a_2} + \frac{a_1b_2}{a_2b_1} + \frac{a_2b_1}{a_1b_2} \quad (2b)$$

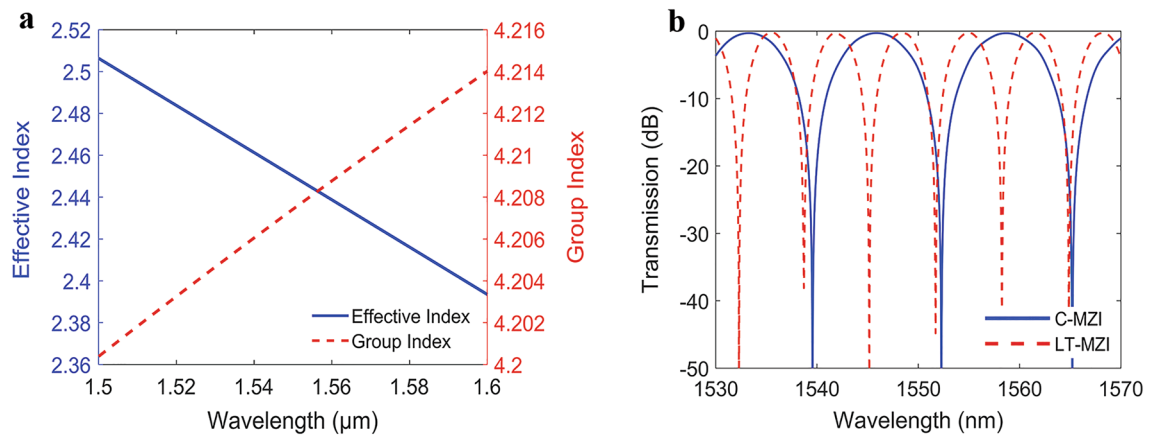


Figure 2. (a) Effective index and group index versus wavelength for the fundamental TE like mode of the (500nm x 220nm) strip waveguide obtained from mode solver and (b) output transmission spectra versus wavelength of both LT-aMZI and C-aMZI for path length differences $\Delta L = 44.7 \mu\text{m}$.

where α_1, b_1 are the forward and cross coupling coefficients of the first DC and α_2, b_2 are the forward and cross coupling coefficients of the second DC. Also, φ_1 and φ_2 are the phase shifts of the upper and lower arms of the interferometer, respectively. We here focus on asymmetric (or unbalanced) MZI, i.e. arms with different lengths L_1 and L_2 and with identical waveguides at both arms, i.e. $\beta_1 = \beta_2 = \beta$. Hence, $\varphi_1 = \beta L_1$, $\varphi_2 = \beta L_2$ and $\Delta\varphi = \varphi_2 - \varphi_1 = \beta \Delta L$ with $\Delta L = L_2 - L_1$ is the interferometer path length difference.

From Eq. (1) we can simply derive the main parameters of the LT-aMZI which are the resonance wavelength (λ_{res}), free spectral range (FSR) and full width half maximum (FWHM) as:

$$\lambda_{\text{res}} = \frac{2n_{\text{eff}} \Delta L}{q} \quad (3a)$$

$$\text{FSR}_{\text{LT-aMZI}} = \frac{\lambda^2}{2n_g \Delta L} \quad (3b)$$

$$\text{For } a_1 = a_2 = b_1 = b_2 = \frac{1}{\sqrt{2}}, H = 0:$$

$$\text{FWHM}_{\text{LT-aMZI}} \approx \frac{\text{FSR}_{\text{LT-aMZI}}}{\pi} \quad (3c)$$

with q an integer number, n_{eff} and n_g are the waveguide mode effective index and group index, respectively. Note that, FWHM is the spectral width $\Delta\lambda$ with transmission greater than or equal to $T_{\text{max}}/2$, which can be derived from Eq. (1) using $T(\lambda_{\text{res}} + \frac{\Delta\lambda}{2}) = \frac{T_{\text{max}}}{2}$.

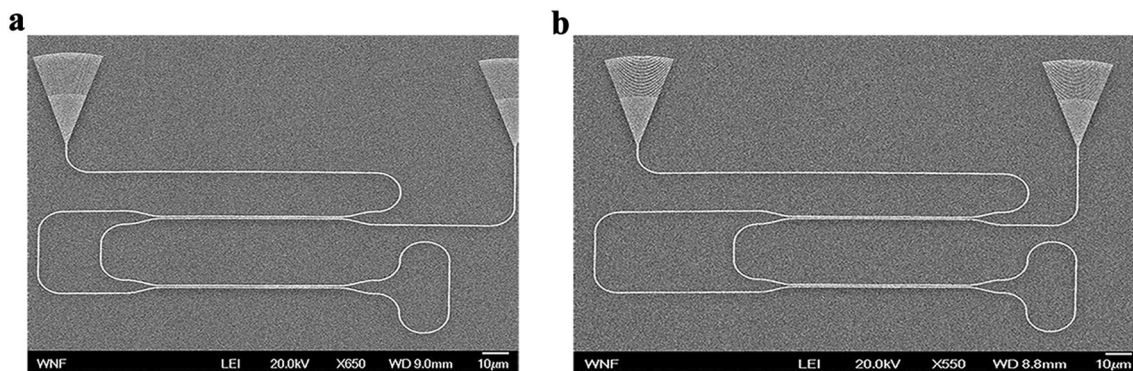
Figure 1c shows the change in the output transmission due to change in the phase difference of both C-MZI and LT-MZI with $\alpha_1 = b_1 = \alpha_2 = b_2 = 1/\sqrt{2}$, i.e. 3-dB directional couplers. It can be seen that, LT-MZI have higher rate of change compared to C-MZI, specifically two times higher. Due to this characteristic LT-aMZI can achieve the same FSR of the C-aMZI using half its path length difference (ΔL). Also, the FWHM of the LT-aMZI is half that of C-aMZI with the same path length difference, because the FSR of the LT-aMZI is half that of C-aMZI. Reducing the FWHM of the interferometer is useful in many applications such as sensors and modulators.

Designs and simulations. We use the quasi-TE mode of the standard SOI strip waveguide with width $w = 500 \text{ nm}$ and thickness $h = 220 \text{ nm}$ and silicon dioxide cladding to construct our interferometer designs. We have performed modal analysis for this waveguide's TE mode using finite difference eigenmode solver³² to get its effective and group index over the wavelength, see Fig. 2a. This waveguide width, $w = 500 \text{ nm}$, is used as it exhibits the least bend and roughness loss while still supporting a single mode.

Using our proposed LT-aMZI, we demonstrate four different designs with different path length differences (ΔL) shown in Table 1. These devices are suitable for optical filtering as well as wavelength de-multiplexing (WDM) applications. We compare these designs with C-aMZI of the same path length difference ΔL . When simulated the C-aMZI y-junctions rather than DCs were used to split and combine the power to and from the interferometer arms, denoted C-aMZI_y. This C-aMZI_y is used when comparing with our LT-aMZI as it is more practical due to the even splitting of the y-junction over broadband. Lumerical Interconnect software tool was mainly used in devices simulations as it is more computationally efficient when compared to 3D FDTD simulations. Interconnect uses scattering matrices of optical components to determine the transfer function of photonic integrated circuits (PICs). In addition, some results have been verified with analytical modeling Eq. (1) showing a very good matching.

Figure 2b shows the Interconnect simulation results of our proposed LT-aMZI and the corresponding C-aMZI_y simulation with $\Delta L = 44.7 \mu\text{m}$. From this result we can see that, as mentioned before, for the same

	$w_1 = w_2$	ΔL	FSR
Design 1	500 nm	44.7 μm	6.4 nm
Design 2	500 nm	89.4 μm	3.2 nm
Design 3	500 nm	178.8 μm	1.6 nm
Design 4	500 nm	357.6 μm	0.8 nm

Table 1. LT-aMZI designs dimensions and FSR.**Figure 3.** SEM photos of the fabricated LT-aMZIs: (a) with $\Delta L = 44.7 \mu\text{m}$, (b) with $\Delta L = 89.4 \mu\text{m}$.

interferometer path length difference ΔL the FSR of the LT-aMZI is half that of the C-aMZI. The DC and y-junction used in the simulations are optimized designs from Lumerical E-Beam Compact Model Library (CML)³³ that result in even power splitting at both outputs over 100 nm bandwidth around 1.55 μm wavelength.

Measurements and characterization. The dimensions of the fabricated LT-aMZIs designs are included in Table 1. The designs were fabricated at the UW NNCI Washington Nanofabrication Facility using Electron Beam lithography³⁴ on standard SOI wafers with silicon device layer of 220 nm. We fabricated three copies for each design to account for the fabrication tolerance. Figure 3a,b show SEM photos of the fabricated LT-aMZIs. Note that, the SEM photos are taken before depositing the SiO_2 clad. As can be seen, bend waveguide loop is crucial in determining the device footprint thus, LT-MZI structure is favorable over the Michelson interferometer where two loop mirrors are needed and hence will increase the footprint significantly. A tunable laser is used to span the wavelength region from 1500 to 1600 nm. A polarization maintaining fiber array containing 4 fibers separated by 127 μm is used to couple light in and out of the chip through the grating couplers while a detector is used to measure the output power from the fibers. The GC used is also from the library in³³. A typical SOI MZI have around 0.5 dB losses (with arms' length in micrometer dimensions)^{35,36} and we can expect roughly that our device losses will be twice that value.

The measurement results of the fabricated designs are compared with different modelling methods to ensure the feasibility of the proposed LT-aMZI structure. Figure 4a shows the device output power spectrum of the fabricated and characterized LT-aMZI Design1 with $\Delta L = 44.7 \mu\text{m}$ together with the Interconnect simulation, and analytical model from Eq. (1). Note that we have added the device IL to the Interconnect and analytical model results. The results show very good agreement among the different modelling methods. The FSR of the different modelling methods is listed in Table 2, showing less than 2.2% difference among the different modelling methods.

As mentioned above, the four designs, $\Delta L = 44.7 \mu\text{m}$, 89.4 μm , 178.8 μm and 357.6 μm , were fabricated with three copies for each design to account for the fabrication tolerances. Figure 4b shows the resonance wavelengths of the LT-aMZI as calculated from the different modelling methods for the same design $\Delta L = 44.7 \mu\text{m}$ with error-bars showing the variations due to fabrication tolerances. Overall, it can be seen that the different modelling methods have good matching with the experimental results with deviation that is lying within the fabrication tolerances. Exact matching is not satisfied for two main reasons. Firstly, the used refractive indices for the silicon and silicon dioxide in Interconnect simulations are not exactly the same as the real refractive indices used in the fabrication of the devices. Secondly, is the dimension mismatch between the devices dimensions on the layout and the fabricated dimensions. Hence, the effective, group index of the waveguide mode, the lengths of the interferometer components and accordingly the resonant wavelengths and FSR will not be matched. We will stick to Interconnect simulations in the rest of the paper because, as mentioned above, it is computationally efficient, especially as the interferometer length is increased.

Figure 4c,d show the measured output power of the fabricated LT-aMZI designs together with the simulation results of Interconnect after adding to this simulation results the insertion loss from the measured data. The measured data are from the samples that best fit the Interconnect simulations. Table 3 shows the FSR determined from simulations and measurements showing less than 2.6% difference among them at 1.55 μm wavelength for the four designs.

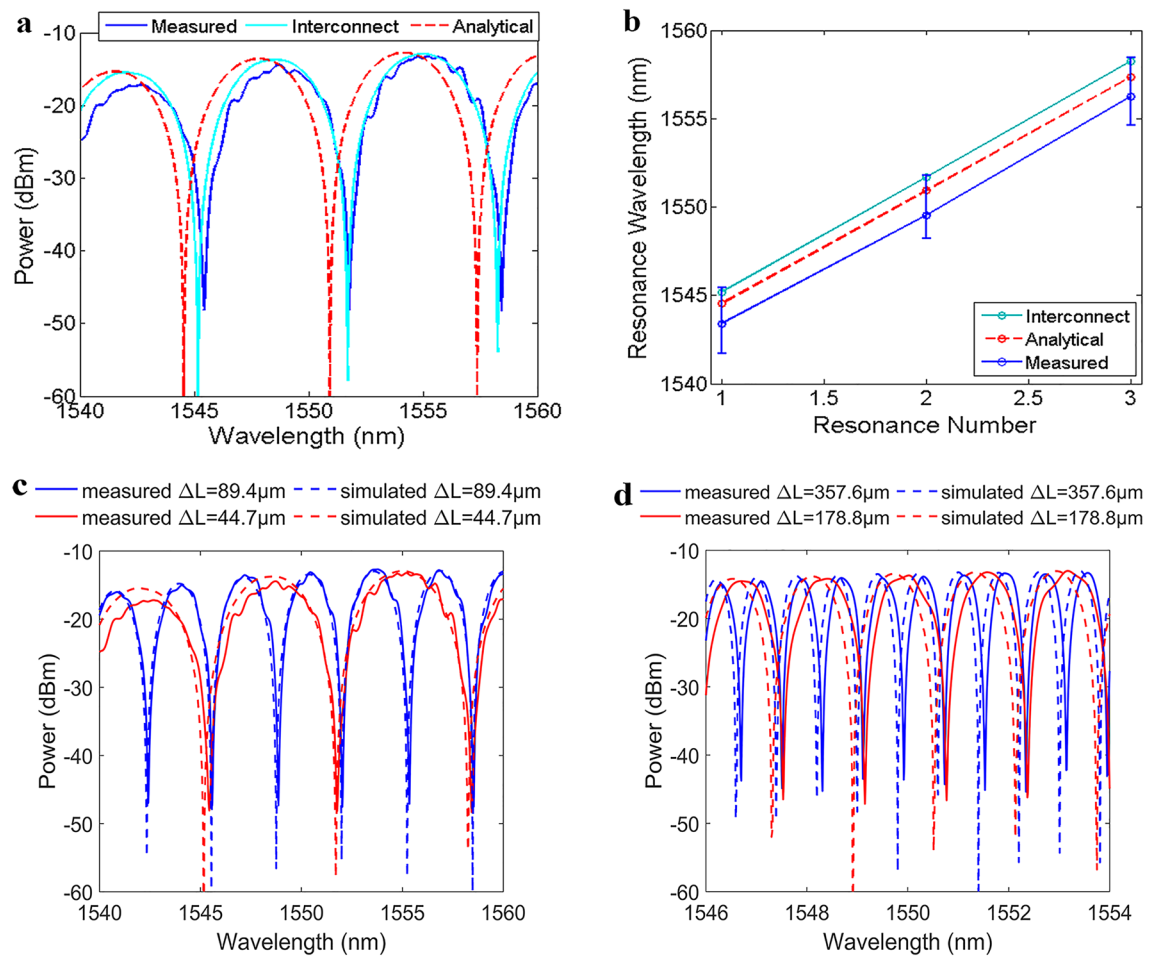


Figure 4. Comparison of the: (a) output power versus wavelength and, (b) resonance wavelengths from measured, Interconnect and analytical modelling of the LT-aMZI with $\Delta L = 44.7 \mu\text{m}$. The measured (solid) and simulated (dotted) output power spectra versus wavelength of the LT-aMZI designs with path length differences: (c) $\Delta L = 44.7 \mu\text{m}$ (red) and $\Delta L = 89.4 \mu\text{m}$ (blue) and (d) $\Delta L = 178.8 \mu\text{m}$ (red) and $\Delta L = 357.6 \mu\text{m}$ (blue).

	FSR (nm)	Difference (%)
Measured	6.490	–
Interconnect	6.440	0.770
Analytical	6.348	2.192

Table 2. Calculated FSR from measurements, Interconnects, and analytical model of the LT-aMZI with $\Delta L = 44.7 \mu\text{m}$.

	FSR simulation	FSR measurement	Difference (%)
Design 1	6.56 nm	6.66 nm	1.5
Design 2	3.24 nm	3.17 nm	2.2
Design 3	1.62 nm	1.6 nm	1.25
Design 4	0.81 nm	0.79 nm	2.53

Table 3. Calculated FSR from simulations and measurements near $1.55 \mu\text{m}$ of the four different LT-aMZI designs and the difference percentage.

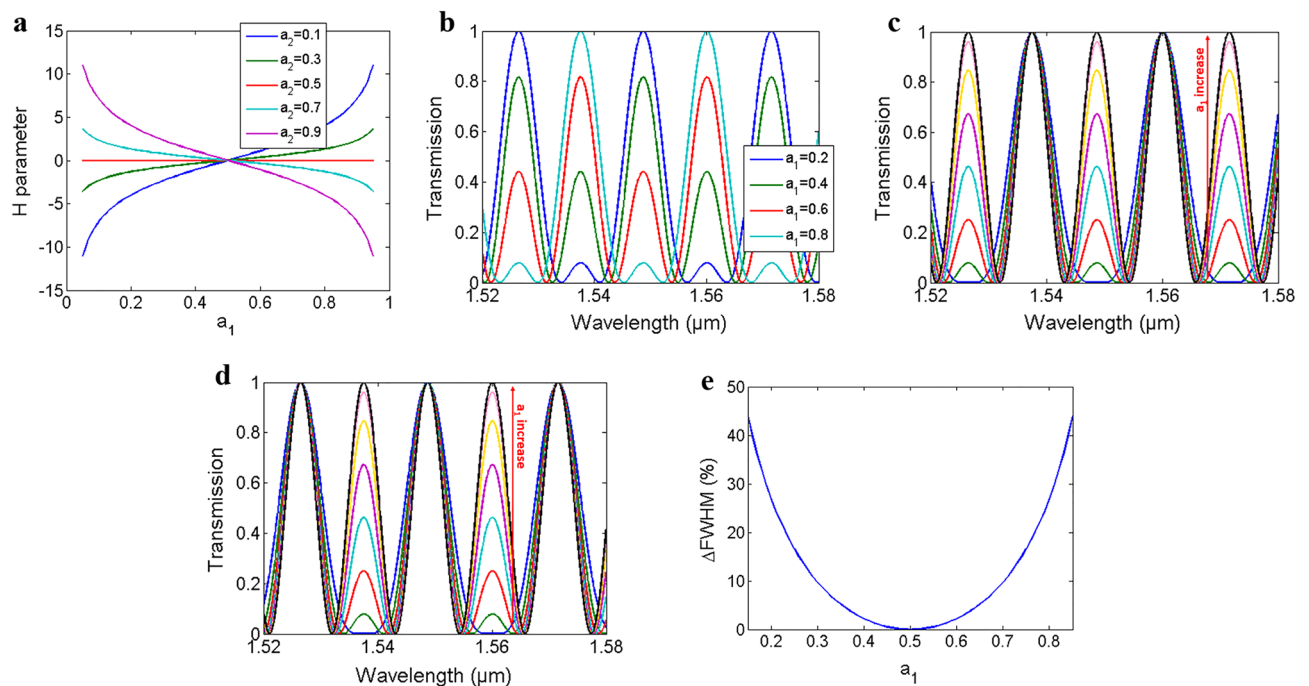


Figure 5. (a) H parameter versus a_1 coefficient at different a_2 . Transmission spectrum versus wavelength of SOI waveguide TE mode at $w = 500$ nm and $\Delta L = 25.4$ μm with: (b) $a_2 = 0.8$ at different a_1 , (c) at different a_1 with $a_2 = a_1$ and (d) at different a_1 with $a_2 = 1 - a_1$ where a_1 increase from 0.15 to 0.5 with 0.05 step as indicated by the arrow. (e) Percentage change of the main loop FWHM versus a_1 for part c and d.

Discussion

Spectral tunable filter. Another unique characteristic of our proposed LT-MZI is that its transmission spectrum can be tuned using the DCs coupling coefficients, working as spectral tunable filter. While this effect is mentioned in³⁰ however, they just investigated three sets $\langle a_1 - a_2 \rangle$ of DCs coefficients and they studied the effect of fabrication tolerances for this specific sets. Here, we discuss the different possible trends of the LT-MZI transmission spectrum which occur due to specific relation between DC_1 and DC_2 coupling coefficients and which are of interest for spectral filter applications.

In the previous sections we focused on LT-MZI with 3-dB DCs ($a_1^2 = a_2^2 = 0.5$). In this case, $H = 0$ and the transmission spectrum reduce to \cos^2 function, see Eqs. (1) and (2). In addition, the FSR and FWHM is half that obtained using a C-MZI with the same path length difference, see Fig. 1c. However, changing the DCs coefficient from this condition will change the H parameter to non-zero values and accordingly the transmission spectrum changes. Figure 5a shows H values at different $a_1 = a_1^2$ and $a_2 = a_2^2$ with $b_1^2 = 1 - a_1^2$ and $b_2^2 = 1 - a_2^2$, i.e. lossless DCs. H is positive when $a_1 > 0.5$ and $a_2 < 0.5$ or vice versa and negative if both $a_1, a_2 > 0.5$ or $a_1, a_2 < 0.5$.

There are mainly three special cases of interest resulting in different trends of the LT-MZI output spectrum. First, changing a_1 while a_2 is fixed at 0.8, see Fig. 5b. It can be seen that, by sweeping DC_1 coupling coefficients the transmission intensity of even and odd resonances are changed inversely and we can flip from a spectrum having only the even resonances to a spectrum having only the odd resonances, thus controlling the relative intensity of the even and odd resonances. Second, changing the DCs coefficients with $a_1 = a_2$, see Fig. 5c, in this case even resonances are always maximum with $T = 1$ while odd resonances intensity can be controlled from 0 to 1 by changing a_1 from 0.15 to 0.5. Finally, changing DCs coefficients such that $a_1 + a_2 = 1$, see Fig. 5d, in this case odd resonances have $T = 1$ while even resonances intensity can be controlled. Note that, in this cases the FSR can be doubled from the case when $a_1 = a_2 = 0.5$. All the transmission spectra of Fig. 5 are obtained using SOI waveguide with $w = 500$ nm and $\Delta L = 25.4$ μm .

As can be seen from the figures, in the two later cases the main loop FWHM changes while changing the DCs coefficients. FWHM is minimum when $a_1 = a_2 = 0.5$ and as a_1 moves far from 0.5 the FWHM increase. Figure 5e shows the FWHM percentage change from the minimum value at $a_1 = a_2 = 0.5$ as a function of a_1 . We can see that for $a_1 = 0.15$ the FWHM increase by 44%. Also note that, while figures shows only a_1 varying from 0.15–0.45 the response is symmetric for a_1 values from 0.5–0.85, i.e. $a_1 = 0.45$ and $a_1 = 0.55$ give the same response as they result in the same H value, see Fig. 5a.

Unlike the transfer matrix method used in³⁰, this behavior can be easily interpreted using our derived closed form expression of Eq. (1). Simply, as DCs coefficients change as H parameter which is a constant shift to the cosine function changes. Accordingly, the part of the cosine below (or above) the zero changes and hence when squaring it the relative intensities of the even and odd resonances changes. Such phenomena does not exist in C-MZI or the Michelson interferometer proposed in²⁹, changing the DCs coefficients in these structures will only change the transmission intensity of the whole spectrum evenly.

Electro-optical modulator. Our proposed LT-MZI design is very promising to enhance the performance of electro-optical modulators that use C-MZI, similar to the Michelson interferometer modulator proposed in²⁹. One of the main electro-optical modulator parameters is the term $V_\pi \times L$ which defines the voltage V_π needed to change the output power of the interferometer with length L from High to Low. Other important parameters are the energy consumption of the modulator and modulation speed (bandwidth). Modulation speed is mainly limited by the RF losses, walk-off between the electrical and optical signal and RC time constant. On the other hand, energy consumption are determined by the RF losses, capacitive loading and the 50 Ω termination resistor. For state-of-the-art modulators such as the ones based on silicon organic hybrid (SOH) platform^{37–40}, the modulator's length can be as small as 500 μm . At such compact length RF losses are reduced^{37,38} and the modulator behave as a lumped element that can be derived without the 50- Ω termination^{38–40}. Accordingly, walk-off is negligible and RC time constant is the main bandwidth limitation, $f_{3\text{dB}} = 1/2\pi RC$ ^{37,38}. Also, the energy consumption is reduced and determined mainly by the capacitive load^{38–40}, which is proportional to CV^2 . Hence, decreasing the capacitance of such modulators will further enhance their performance.

Now assume a symmetric (balanced) interferometer, $L_1 = L_2 = L$, where the applied voltage V changes the interferometer arms effective index and hence switching the output power from high to low. For LT-aMZI and C-aMZI with $a_1 = a_2 = b_1 = b_2 = 1/\sqrt{2}$ we have:

$$T_{LT-aMZI} = \cos^2(\Delta\phi) \quad (4a)$$

$$T_{C-aMZI} = \cos^2\left(\frac{\Delta\phi}{2}\right) \quad (4b)$$

Hence to switch from ON to OFF we need:

$$\Delta\phi = \pi \Rightarrow \frac{2\pi \Delta n_{\text{eff}} L_{C-MZI}}{\lambda} = \pi \Rightarrow L_{C-MZI} = \frac{\lambda}{2\Delta n_{\text{eff}}} \quad (5a)$$

$$\Delta\phi = \frac{\pi}{2} \Rightarrow \frac{2\pi \Delta n_{\text{eff}} L_{LT-MZI}}{\lambda} = \frac{\pi}{2} \Rightarrow L_{LT-MZI} = \frac{\lambda}{4\Delta n_{\text{eff}}} \quad (5b)$$

Δn_{eff} is proportional to the applied ΔV . For the same waveguide configuration and same applied voltage V , both C-MZI and LT-MZI will have the same Δn_{eff} . Hence, Eq. (5) shows that the $V_\pi \times L$ term will be two times smaller for our proposed LT-MZI. This shows that LT-MZI design is more compact ($L_{LT-MZI} = L_{C-MZI}/2$). On the other hand, the capacitance of the modulator expressed by Eq. (6) will also decrease to half the value of the C-MZI ($C_{LT-MZI} = C_{C-MZI}/2$). Accordingly, for compact state-of-the-art modulators this will effectively reduce the energy consumption and increase the modulation speed for the LT-MZI design.

$$C = \epsilon_0 \epsilon_r \frac{h \times L}{d} \quad (6)$$

where ϵ_r is the permittivity of the capacitor dielectric material, d is the conducting plate separation, h is the waveguide thickness and L is the interferometer arm's length.

Optical sensor. The main performance parameter of optical sensors is the figure of merit (FOM) which is defined as⁴¹:

$$FOM = \frac{d\lambda/dn_{\text{med}}}{FWHM} = \frac{S}{FWHM} \quad (7)$$

where S is the wavelength sensitivity and n_{med} is the refractive index of the sensed medium. The resonance wavelengths for LT-aMZI and C-aMZI are:

$$\Delta\phi = q\pi \Rightarrow \lambda_{\text{res},LT-aMZI} = \frac{2}{q}(n_{\text{eff},\text{sens}}L_{\text{sens}} - n_{\text{eff},\text{ref}}L_{\text{ref}}) \quad (8a)$$

$$\frac{\Delta\phi}{2} = q\pi \Rightarrow \lambda_{\text{res},C-aMZI} = \frac{1}{q}(n_{\text{eff},\text{sens}}L_{\text{sens}} - n_{\text{eff},\text{ref}}L_{\text{ref}}) \quad (8b)$$

where $n_{\text{eff},\text{sens}}$, L_{sens} and $n_{\text{eff},\text{ref}}$, L_{ref} are the effective index, arm length of the sensing and reference arm, respectively. Hence, the wavelength sensitivity of both interferometers can be derived to be:

$$S_{LT-aMZI} = \frac{\lambda_{\text{res}}}{(n_{\text{eff},\text{sens}}L_{\text{sens}} - n_{\text{eff},\text{ref}}L_{\text{ref}})} L_{\text{sens}} S_{\text{wg}} \quad (9a)$$

$$S_{C-aMZI} = \frac{\lambda_{\text{res}}}{(n_{\text{eff},\text{sens}}L_{\text{sens}} - n_{\text{eff},\text{ref}}L_{\text{ref}})} L_{\text{sens}} S_{\text{wg}} \quad (9b)$$

where $S_{wg} = dn_{eff}/dn_{med}$ is the sensing arm waveguide sensitivity. So, both LT-aMZI and C-aMZI configuration have the same wavelength sensitivity S for the same waveguide structure and same dimensions. This sensitivity increase as $L_{sens} \rightarrow (n_{ref}/n_{sens}) \times L_{ref}$. On the other hand, FWHM is expressed as:

$$FWHM = \frac{FSR}{\pi} \quad (10)$$

$$\text{with } FSR_{LT-aMZI} = \frac{\lambda^2}{2(n_{eff,sens}L_{sens} - n_{eff,ref}L_{ref})} \quad (11a)$$

$$\text{and } FSR_{C-aMZI} = \frac{\lambda^2}{(n_{eff,sens}L_{sens} - n_{eff,ref}L_{ref})} \quad (11b)$$

The FWHM of LT-aMZI is half that of C-aMZI, while both increase as $L_{sens} \rightarrow (n_{ref}/n_{sens}) \times L_{ref}$. Accordingly:

$$FOM_{LT-aMZI} = \frac{S}{FWHM} = \frac{2\pi S_{wg}L_{sens}}{\lambda} = 2FOM_{C-aMZI} \quad (12)$$

FOM of LT-aMZI is double that of C-aMZI with both proportional to sensing arm length L_{sens} and its waveguide sensitivity S_{wg} . In general, aMZI (or unbalanced MZI) sensor offers advantage over the sMZI. For the symmetric LT-MZI (LT-sMZI) where $L_{sens} = L_{ref} = L$ we have:

$$S_{LT-sMZI} = \frac{\lambda_{res}}{\Delta n_{eff}} S_{wg} \quad (13a)$$

$$FSR_{LT-sMZI} = \frac{\lambda^2}{2\Delta n_{eff}L} \quad (13b)$$

$$FOM_{LT-sMZI} = \frac{2\pi S_{wg}L}{\lambda} \quad (13c)$$

Hence, for the LT-sMZI the sensitivity is independent of L while FWHM decrease as L increase and FOM expression is the same as in the case of LT-aMZI. However, in the asymmetric MZI sensor you can engineer both S and FOM independently using L_{ref} and L_{sens} , Eq. (9) and Eq. (12), and independent of the used waveguide structures (i.e. S_{wg} and n_{eff}), while in the case of symmetric MZI the sensor sensitivity is determined only by the waveguide structure, Eq. (13a). This is also an advantage over ring resonator sensors.

Conclusion

In conclusion a LT-aMZI structure using the popular SOI technology have been proposed, this design is a compact version of the widespread C-aMZI. Four designs for optical filters and WDM applications with different FSR were implemented and characterized both numerically and experimental as well as analytically using our derived compact model. The different modelling techniques show good matching with the experimental results of the fabricated devices. It was also shown that, our LT-MZI spectrum can be tuned by changing its DCs coefficients for spectral tunable filter application. Finally, using our compact model the interferometer proved to have better performance when compared with the widespread C-MZI in sensing and modulation applications, and we also demonstrated that LT-aMZI sensor configuration is preferable over the LT-sMZI.

Materials and methods

The designs were fabricated at the UW NNCI Washington Nanofabrication Facility using Electron Beam lithography³⁴ on standard SOI wafers with silicon device layer of 220 nm. We fabricated three copies for each design to account for the fabrication tolerance.

The device measurements were performed by the team of Lukas Chrostowski at The University of British Columbia and by Maple Leaf Photonics^{42,43}. A tunable laser is used to span the wavelength region from 1500 to 1600 nm. A polarization maintaining fiber array containing 4 fibers separated by 127 μm is used to couple light in and out of the chip through the grating couplers while a detector is used to measure the output power from the fibers. Also note, that the SEM photos are taken before depositing the SiO₂ clad.

Received: 2 August 2021; Accepted: 5 January 2022

Published online: 04 March 2022

References

1. Poulton, C. V. *et al.* Coherent solid-state LIDAR with silicon photonic optical phased arrays. *Opt. Lett.* **42**, 4091–4094 (2017).
2. Wangüemert-Pérez, J. G. *et al.* [INVITED] Subwavelength structures for silicon photonics biosensing. *Opt. Laser Technol.* **109**, 437–448 (2019).
3. Fard, S. T. *et al.* Label-free Silicon Photonic Biosensors for Use in Clinical Diagnostics. In *Silicon Photonics VIII*, Vol. 8629, 862909 (International Society for Optics and Photonics, 2013).
4. Capmany, J. & Novak, D. Microwave photonics combines two worlds. *Nat. Photonics* **1**, 319–330 (2007).

5. Burla, M. *et al.* Integrated waveguide Bragg gratings for microwave photonics signal processing. *Opt. Express* **21**, 25120–25147 (2013).
6. Porzi, C., Serafino, G., Velha, P., Ghelfi, P. & Bogoni, A. Integrated SOI high-order phase-shifted Bragg grating for microwave photonics signal processing. *J. Lightwave Technol.* **35**, 4479–4487 (2017).
7. Compact broadband polarization beam splitter based on multimode interference coupler with internal photonic crystal for the SOI platform—IEEE J. Magazine. <https://ieeexplore.ieee.org/abstract/document/8598856>.
8. Nambiar, S., Sethi, P. & Selvaraja, S. K. Grating-assisted fiber to chip coupling for SOI photonic circuits. *Appl. Sci.* **8**, 1142 (2018).
9. Preite, M. V. *et al.* Mach-Zehnder-based 1×16 multiplexer in SOI and analysis of phase noise properties. In *Optical Fiber Communication Conference (2018), Paper M4H.3* M4H.3 (Optical Society of America, 2018). <https://doi.org/10.1364/OFC.2018.M4H.3>.
10. Lin, Z. & Shi, W. Broadband, low-loss silicon photonic Y-junction with an arbitrary power splitting ratio. *Opt. Express* **27**, 14338–14343 (2019).
11. imec-ePIXfab SiPhotonics Passives. http://www.europractice-ic.com/SiPhotonics_technology_imec_passives.php.
12. Duy, H. T. *et al.* A numerical simulation design demonstrated in system level of 40 gbps silicon two-mode demultiplexer using slot phase shifter. In *2019 19th International Symposium on Communications and Information Technologies (ISCIT)* 584–589 (2019). <https://doi.org/10.1109/ISCIT.2019.8905181>.
13. Bogaerts, W. & Selvaraja, S. K. 13—Silicon-on-insulator (SOI) technology for photonic integrated circuits (PICs). In *Silicon-on-insulator (SOI) technology* (eds Kononchuk, O. & Nguyen, B. Y.) 395–434 (Woodhead Publishing, 2014). <https://doi.org/10.1533/9780857099259.2.395>.
14. Kumar, S., Singh, G. & Bisht, A. 4×4 Signal router based on electro-optic effect of Mach-Zehnder interferometer for wavelength division multiplexing applications. *Opt. Commun.* **353**, 17–26 (2015).
15. Lu, L. *et al.* 16×16 non-blocking silicon optical switch based on electro-optic Mach-Zehnder interferometers. *Opt. Express* **24**, 9295–9307 (2016).
16. Chen, S., Shi, Y., He, S. & Dai, D. Low-loss and broadband 2×2 silicon thermo-optic Mach-Zehnder switch with bent directional couplers. *Opt. Lett.* **41**, 836–839 (2016).
17. Amin, R. *et al.* An ITO-based Mach-Zehnder modulator with lateral MOS-capacitor on SOI platform. In *Frontiers in Optics + Laser Science APS/DLS (2019), Paper JW3A.67* JW3A.67 (Optical Society of America, 2019). <https://doi.org/10.1364/FIO.2019.JW3A.67>.
18. Power-efficient carrier-depletion SOI Mach-Zehnder modulators for 4×25 Gbit/s operation in the O-band. <https://www.spiedigitallibrary.org/conference-proceedings-of-spie/9367/93670D/Power-efficient-carrier-depletion-SOI-Mach-Zehnder-modulators-for-4x25Gbit/> <https://doi.org/10.1117/12.2078364.short?SSO=1>.
19. Palmer, R. *et al.* Low power Mach-Zehnder modulator in silicon-organic hybrid technology. *IEEE Photonics Technol. Lett.* **25**, 1226–1229 (2013).
20. Leuerman, J. *et al.* Towards photonic biosensing using a three-port mach-zehnder interferometer in a silicon nitride platform. (2018).
21. Qin, K., Hu, S., Retterer, S. T., Kravchenko, I. I. & Weiss, S. M. Slow light Mach-Zehnder interferometer as label-free biosensor with scalable sensitivity. *Opt. Lett.* **41**, 753–756 (2016).
22. Lambeck, P. V. Integrated optical sensors for the chemical domain. *Meas. Sci. Technol.* **17**, R93 (2006).
23. Mortimore, D. B. Fiber loop reflectors. *J. Lightwave Technol.* **6**, 1217–1224 (1988).
24. Song, J. *et al.* Loop coupled resonator optical waveguides. *Opt. Express* **22**(20), 24202–24216 (2014).
25. Millar, C. A., Harvey, D. & Urquhart, P. Fibre reflection mach-zehnder interferometer. *Opt. Commun.* **70**, 304–308 (1989).
26. Afifi, A. E. *et al.* Novel silicon-on-insulator Michelson interferometer for optical filtering and wavelength demultiplexing applications. In *Silicon Photonics XIV*. Vol. 10923. (International Society for Optics and Photonics, 2019).
27. Jiang, X. *et al.* Wavelength and bandwidth-tunable silicon comb filter based on Sagnac loop mirrors with Mach-Zehnder interferometer couplers. *Opt. Express* **24**, 2183–2188 (2016).
28. Song, J. *et al.* Silicon nanowire-based thermo-optical tunablereflector. *Int. J. Inf. Electron. Eng.* **2**(6), 853 (2012).
29. Patel, D. *et al.* High-speed compact silicon photonic Michelson interferometric modulator. *Opt. Express* **22**, 26788–26802 (2014).
30. Troia, B., De Leonardi, F. & Passaro, V. M. Cascaded ring resonator and Mach-Zehnder interferometer with a Sagnac loop for Vernier-effect refractive index sensing. *Sens. Actuators B Chem.* **240**, 76–89 (2017).
31. PIC Design and Simulation Software—Lumerical INTERCONNECT. Lumerical <https://www.lumerical.com/products/interconnect/>.
32. Optical Waveguide Design Software—Lumerical MODE Solutions. Lumerical <https://www.lumerical.com/products/mode-solutions/>.
33. Chrostowski, L. SiEPIC EBeam PDK & Library, for SiEPIC-Tools and KLayout: lukasc-ubc/SiEPIC_EBeam_PDK. https://github.com/lukasc-ubc/SiEPIC_EBeam_PDK (2019).
34. Equipment/Capabilities|UW NNCI Washington Nanofabrication Facility website (2018). <https://www.wnf.washington.edu/about/equipment/>. (Accessed 15 Apr 2019).
35. Bogaerts, W. *et al.* Silicon-on-insulator spectral filters fabricated with CMOS technology. *IEEE J. Sel. Top. Quantum Electron.* **16**(1), 33–44 (2010).
36. Horst, F. *et al.* Cascaded Mach-Zehnder wavelength filters in silicon photonics for low loss and flat pass-band WDM (de-) multiplexing. *Opt. Express* **21**(10), 11652–11658 (2013).
37. Alloatti, L. *et al.* 100 GHz silicon-organic hybrid modulator. *Light Sci. Appl.* **3**(5), e173 (2014).
38. Leuthold, J. *et al.* Silicon-organic hybrid electro-optical devices. *IEEE J. Sel. Top. Quantum Electron.* **19**(6), 114–126 (2013).
39. Koeber, S. *et al.* Femtojoule electro-optic modulation using a silicon-organic hybrid device. *Light Sci. Appl.* **4**(2), e255 (2015).
40. Palmer, R. *et al.* High-speed, low drive-voltage silicon-organic hybrid modulator based on a binary-chromophore electro-optic material. *J. Lightwave Technol.* **32**(16), 2726–2734 (2014).
41. Gao, Y., Gan, Q., Xin, Z., Cheng, X. & Bartoli, F. J. *Plasmonic Mach-Zehnder Interferometer for Ultrasensitive On-Chip Biosensing*. (2011) <https://doi.org/10.1021/nn2034204>.
42. Microsystems and Nanotechnology (MiNa) Group—The University of British Columbia.
43. Maple Leaf Photonics website. <http://mapleleafphotonics.com/>. (Accessed on 15 Apr 2019).

Acknowledgements

This work was made possible by a NPRP award [NPRP 7-456-1-085] from the Qatar National Research Fund (member of the Qatar Foundation). The statements made herein are solely the responsibility of the authors.

Author contributions

A.E.A. conceived the basic idea and validated the concept of operation through computer-aided simulations. R.S.E.S. developed a theoretical model for the device, designed the layout of the device for fabrication, analyzed the data and results and wrote the paper. M.M.B. helped in writing and revising the manuscript. M.A.S. supervised the entire project. All the authors contributed to the general discussion and revision of the manuscript.

Competing interests

The authors declare no competing interests.

Additional information

Correspondence and requests for materials should be addressed to M.A.S.

Reprints and permissions information is available at www.nature.com/reprints.

Publisher's note Springer Nature remains neutral with regard to jurisdictional claims in published maps and institutional affiliations.



Open Access This article is licensed under a Creative Commons Attribution 4.0 International License, which permits use, sharing, adaptation, distribution and reproduction in any medium or format, as long as you give appropriate credit to the original author(s) and the source, provide a link to the Creative Commons licence, and indicate if changes were made. The images or other third party material in this article are included in the article's Creative Commons licence, unless indicated otherwise in a credit line to the material. If material is not included in the article's Creative Commons licence and your intended use is not permitted by statutory regulation or exceeds the permitted use, you will need to obtain permission directly from the copyright holder. To view a copy of this licence, visit <http://creativecommons.org/licenses/by/4.0/>.

© The Author(s) 2022